RSC Advances

PAPER

View Article Online
View Journal | View Issue

Cite this: *RSC Adv.*, 2026, **16**, 25423

Investigation of the structural, optical, and electrical properties of the $(CH_3NH_3)_3(SbCl_5)\cdot Cl$ compound

N. Chakchouk,[a] H. Khachroum,[e] M. A. Ben Yazeed,[b] A. A. Awhida,[c] M. S. M. Abdelbaky,[de] S. García Granda[e] and A. Ben Rhaiem *[a]

Single crystals of $(CH_3NH_3)_3(SbCl_5)\cdot Cl$ were synthesized *via* slow evaporation. X-ray diffraction revealed a monoclinic structure (space group $P2_1/m$) with lattice parameters a = 13.0073 Å, b = 8.0388 Å, c = 15.1149 Å, and β = 95.669°. Optical studies indicated a direct band gap of 2.34 eV. Photoluminescence studies showed a broad emission centered at 600–610 nm with a full width at half-maximum of 100–150 nm, suggesting self-trapped excitons. Impedance spectroscopy from 313 to 363 K and 0.1 to 10^6 Hz showed that the direct current conductivity increased from 5.26 × 10^{-7} Ω^{-1} cm^{-1} at 313 K to 7.20 × 10^{-5} Ω^{-1} cm^{-1} at 363 K, following Arrhenius behavior with an activation energy of 0.27 eV. Relaxation frequency exhibited thermally activated behavior with an activation energy of 0.49 eV. Alternating current conductivity obeyed Jonscher's universal power law, with the exponent ranging from 0.53 to 0.76 and increasing with temperature. Charge transport was governed by non-overlapping small polaron tunneling. The temperature evolution of the imaginary modulus peak revealed a stretching exponent varying between 0.47 and 0.48, confirming a thermally activated non-Debye relaxation mechanism. A correlation between the ionic conductivity and crystallographic channels along the 101 direction was established, highlighting the potential for fabricating optoelectronic and ionic devices.

Received 3rd February 2026
Accepted 10th April 2026

DOI: 10.1039/d6ra00964f

rsc.li/rsc-advances

1. Introduction

Perovskite materials combine the complementary physical and chemical advantages of both their organic and inorganic components. The organic moiety contributes structural flexibility, high polarizability, and strong luminescence efficiency, while the inorganic framework provides dielectric behavior, thermal robustness, and favorable electrical properties that can transform insulating systems into semiconductors. As a result, this class of perovskite structures has attracted significant interest for photovoltaic applications. Extensive research efforts have led to a rapid increase in solar cell efficiency, with quantum yields rising from 3.8% in 2009 (ref. 1) to 22% in 2016,[2] making perovskite-based solar cells one of the fastest-developing and most cost-effective photovoltaic technologies to date. During the past decade, hybrid perovskites have gained considerable attention as a new generation of materials for optoelectronic devices. Perovskite-based solar cells have reached power conversion efficiencies approaching 25%,[3] placing them on par with established commercial technologies, such as polysilicon, cadmium telluride (CdTe), and copper indium gallium selenide (CIGS) solar cells.[4]

This strong performance is attributed to their outstanding photovoltaic characteristics, including broad optical absorption with a relatively high absorption coefficient,[5] efficient charge transport associated with long carrier lifetimes,[6] extended diffusion lengths,[7] and straightforward fabrication processes that rely on simple and cost-effective techniques.[8] However, the search for lead-free, ecologically friendly materials for next-generation optoelectronic devices has placed increased emphasis on hybrid halide compounds, especially those that include antimony(III) centers.[9] These systems exhibit noticeable local aberrations that significantly impact their electronic configuration and result in exceptional dielectric and photophysical characteristics due to the stereoactive $5s^2$ lone pair of Sb^{3+}.[10]

Zero-dimensional (0D) antimony halides stand out among them due to their broadband photoluminescence, which is produced by the self-trapped excitons (STEs) generated by strong electron–phonon interactions inside rigid polyhedral frameworks. They are appealing options for light-emitting and photonic applications due to their high photoluminescence

[a]*Laboratory LaSCOM, Faculty of Sciences of Sfax, University of Sfax, BP1171, 3000, Sfax, Tunisia*
[b]*Department of Physics, Faculty of Science, University of Alasmarya Islamic, Zliten, Libya*
[c]*Higher Institute of Engineering Technologies, Zliten, Libya*
[d]*Department of Physical Chemistry, Faculty of Chemical Science, University of Salamanca, E-37008, Salamanca, Spain*
[e]*Department of Physical and Analytical Chemistry, Oviedo University-CINN, 33006, Oviedo, Spain. E-mail: abdallahrhaiem@yahoo.fr*

quantum yields (PLQYs).[11] Structural and compositional design can be used to precisely control the optoelectronic performance of Sb(III)-based hybrids. The band gap and emission profile can be changed by adjusting halide anions or by fine-tuning the organic cation, allowing exact control over charge transfer, color, and absorption properties.[12] Numerous investigations have shown that the addition of polar or chiral organic cations enhances nonlinear optical responses by promoting non-centrosymmetric structures with second-harmonic-generation (SHG) activity. Similarly, anisotropic emission behavior appropriate for polarized light or tunable-emission devices is produced *via* the controlled orientation of organic moieties.

Other perovskite-type metallic and hybrid halides, such as bismuth halides,[13] orthorhombic chromites[14] and $LiNbO_3$-type oxides,[15] exhibit similar structure–property relationships. These findings highlight crystal symmetry and the nature of cation–anion interactions as fundamental parameters for engineering tailored optical and dielectric responses. Sb(III) hybrids have diverse electrical and dielectric characteristics that go beyond optical tunability. These behaviors include polarization relaxation, high permittivity, and frequency dispersion. Dipolar cations' dynamic reorientation and the inorganic sublattice's polarizability are the sources of these characteristics. A number of antimony-based systems have been reported to exhibit reversible spontaneous polarization, indicating ferroelectric-like switching phenomena that hold significant potential for applications in sensing technologies and memory storage.[16,17] Interest in incorporating Sb(III) halide frameworks into devices that combine optical, electrical, and thermal functions has increased as a result of these multifunctional qualities.

In this study, a novel single-crystalline antimony-based hybrid, $(CH_3NH_3)_3(SbCl_5)\cdot Cl$, was created *via* slow evaporation and examined utilizing complementary theoretical and experimental approaches. This compound was specifically designed and selected for its promising multifunctional potential in next-generation optoelectronic and dielectric applications. Based on its structural features and preliminary property assessments, the potential usages of $(CH_3NH_3)_3(SbCl_5)\cdot Cl$ single crystals include solid-state lighting and white-light emission, where its broadband photoluminescence attributed to STEs offers a rare-earth-free alternative to phosphor-converted white LEDs; UV-visible photodetection, where its direct optical band gap and efficient charge transport are leveraged for sensitive, low-power sensing applications; X-ray and radiation scintillation, which is enabled by the high atomic number of antimony coupled with strong luminescence efficiency, for medical imaging and security screening; ferroelectric and dielectric memory devices, which is supported by the switchable polarization induced by polar methylammonium cations and the stereoactive lone pair of Sb^{3+}; and nonlinear optical applications, where non-centrosymmetric structural motifs may facilitate second-harmonic generation for laser frequency conversion.

The importance of $(CH_3NH_3)_3(SbCl_5)\cdot Cl$ over other perovskite-type materials is multifaceted. Compared to conventional lead-based perovskites, such as $MAPbI_3$, this material offers critical advantages in environmental safety and reduced toxicity, as antimony is significantly less hazardous than lead, thereby addressing regulatory and sustainability concerns. It also exhibits enhanced thermal and moisture stability, extending the device lifetime, while its STE-mediated broadband emission provides superior color rendering for lighting applications compared to the narrow emission profiles of lead halides. Compared to other Sb/Bi-based hybrids, the optimized $[SbCl_5]^{2-}$ anionic framework, combined with dynamic methylammonium cations, yields a balanced trade-off between structural rigidity and polarizability, enhancing both optical and dielectric responses. Furthermore, its band gap and emission profile can be finely tuned *via* halide substitution or organic cation engineering, offering greater design flexibility than many reported antimony halides. The simultaneous presence of strong photoluminescence, dielectric relaxation, and potential ferroelectric behavior in a single phase enables integrated optoelectronic–dielectric devices—a rarity among reported Sb-based systems. Finally, compared to conventional inorganic semiconductors such as Si or GaAs, $(CH_3NH_3)_3(SbCl_5)\cdot Cl$ benefits from solution-processability and low-temperature fabrication, enabling scalable, cost-effective production, as well as mechanical flexibility compatible with wearable and conformable electronics.

To validate these properties, optical (UV-vis and photoluminescence) and electrical analyses were carried out. To identify the suitable model governing the conduction mechanism, the relationship between crystallographic and electrical properties was also examined. The material exhibits a direct optical band gap in agreement with theoretical predictions, along with strong photoluminescence efficiency and dielectric relaxation characteristics. Combined with its lead-free nature and wide thermal stability range, these features underscore its promise for environmentally sustainable optoelectronic applications. Collectively, these attributes position $(CH_3NH_3)_3(SbCl_5)\cdot Cl$ as a strategically important material in the ongoing transition toward sustainable, high-performance, and multifunctional optoelectronic technologies.

2. Experimental section

2.1. Chemicals

Sigma-Aldrich (St. Louis, MO, USA) provided methylammonium chloride (Sigma-Aldrich, ≥99.0%, cat. no. 539676) and antimony(III) chloride (Sigma-Aldrich, 99.99%, trace metals basis, cat. no. 229978) for the synthesis process. Every reagent was used as received, without going through any further purification procedures. All manipulations were carried out under ambient laboratory conditions (temperature: 22 °C ± 2 °C; relative humidity: 40–60%), unless otherwise specified.

2.2. Preparation of perovskites

Initially, methylammonium antimony chloride was synthesized by dissolving methylammonium chloride (0.203 g, 3 mmol) and antimony chloride (0.228 g, 1 mmol) in 50 mL of deionized water (resistivity: 18.2 MΩ cm, purified using a Milli-Q Integral system, Merck Millipore, Darmstadt, Germany) at room temperature (25 °C ± 1 °C). The resulting aqueous solution

containing the perovskite precursors was allowed to evaporate slowly over several weeks in a covered beaker with a pinhole lid to control the evaporation rate (~0.5 mL per day) under dark conditions to prevent photo-induced degradation. White polyhedral crystals formed after a few days; these crystals were collected by vacuum filtration using Whatman no. 42 filter paper, dried under dynamic vacuum (10^{-2} mbar) for 12 h at 30 °C, and stored in a sealed amber glass vial under an argon atmosphere for the subsequent characterization and analysis.

The single crystals were obtained using the slow evaporation method, which enables gradual crystal growth at room temperature. This approach is simple, cost-effective, and does not require specialized equipment. It produces high-quality, well-formed crystals suitable for X-ray diffraction and allows some control over the crystal size by adjusting the evaporation rate.

Additionally, the method is environmentally friendly, generating minimal chemical waste and avoiding high temperatures or pressures. However, it is time-consuming, often requiring days to weeks, and the crystal quality and size are sensitive to environmental factors such as temperature and humidity. Compared to rapid crystallization or hydrothermal methods, slow evaporation promotes the growth of larger, defect-free crystals ideal for detailed structural studies. To minimize potential disadvantages, we maintained stable room conditions, optimized the solution concentration and solvent volume, and avoided disturbances or vibrations near the growing crystals.

2.3. Technical characterizations

Single-crystal X-ray diffraction (XRD) measurements were carried out using an Agilent Gemini CCD diffractometer mounted on a glass fiber carrying small crystals of the novel compound. Intensity data were collected at room temperature using Mo-Kα radiation (λ = 0.071073 Å) generated by a fine-focus sealed tube operated at 50 kV and 40 mA. Data collection was performed using ω-scans with a scan width of 0.5° and an exposure time of 10 s per frame. A total of 1250 frames were collected over the 2θ range of 3.2° to 27.5°. Absorption corrections were applied using the multi-scan method implemented in the CrysAlis PRO software (version 1.171.38.46, Rigaku Oxford Diffraction, 2015). The crystal structures were solved using SHELXS-97, which employs direct methods for determining initial atomic positions from diffraction data. The structures were subsequently refined using SHELXL, which allows full-matrix least-squares refinement based on F^2, providing accurate anisotropic displacement parameters for non-hydrogen atoms. SHELXT is used as an integrated tool for rapid structure solution, combining the benefits of direct methods with advanced Fourier techniques, speeding up initial structure determination. All refinements were performed within the OLEX2 package,[18–20] which provides a user-friendly interface for managing crystallographic data, visualizing structures, and performing refinements efficiently. The combination of these programs allowed accurate, reproducible, and high-quality structural determination. Hydrogen atoms were positioned geometrically, while Mercury 3.8 was used to generate visual representations of the asymmetric units and crystal structures.[21] Anisotropic displacement parameters are listed in Table S1, partial atomic coordinates and isotropic thermal parameters in Table S2, and selected bond lengths (Å) and angles (°) in Table S3. UV-vis diffuse reflectance spectra were measured at room temperature (25 °C ± 1 °C) using a Shimadzu UV-3101PC spectrophotometer (Shimadzu Corporation, Kyoto, Japan; equipped with an integrating sphere ISR-3100 and $BaSO_4$ as a reference standard), covering a wavelength range of 200–800 nm with a resolution of 0.5 nm, a scan speed of 120 nm min^{-1}, and a slit width of 2.0 nm. Reflectance data were converted to absorbance using the Kubelka–Munk function: $F(R) = (1 - R)^2/2R$, where R is the diffuse reflectance. Photoluminescence (PL) spectra were obtained at room temperature (25 °C ± 1 °C) using a Shimadzu RF-6000 spectrofluorophotometer (Shimadzu Corporation, Kyoto, Japan; equipped with a 150-W xenon flash lamp). Measurements were performed in the solid-state mode using a front-surface illumination geometry. The excitation wavelength was set at 325 nm with slit widths of 5 nm for both excitation and emission. Emission spectra were recorded from 350 to 750 nm at a scan rate of 240 nm min^{-1}. All spectra were corrected for the instrument response using a calibrated reference detector. For impedance analysis, a small portion of $(CH_3NH_3)_3(SbCl_5)\cdot Cl$ was ground into a fine powder using an agate mortar and pestle. The powder was pre-dried at 40 °C under vacuum (10^{-2} mbar) for 6 h to remove adsorbed moisture prior to pelletization. Pellets with a 1.2 mm thickness and a 92% theoretical density were prepared using an 8-mm diameter hydraulic press (Specac Ltd, Orpington, UK; model: Atlas25 T) under a uniaxial pressure of 5 tons (245 MPa) applied for 2 min. The pellets were placed between two copper electrodes (99.9% purity, 10 mm diameter, polished with 1 μm alumina slurry) and coated with silver paint (Agar Scientific, Stansted, UK; conductive silver epoxy, cured at 60 °C for 30 min) to ensure good electrical contact. Transport properties were measured using a Solartron 1260 impedance/gain-phase analyzer (AMETEK Scientific Instruments, Berwyn, PA, USA; equipped with a 1296 dielectric interface) under high vacuum (<10^{-3} mbar) at temperatures from 313 K to 363 K (controlled by an Eurotherm 2216 temperature controller with ±0.5 K stability). Frequency sweeps ranged from 10^{-1} Hz to 10^6 Hz, and an AC voltage of 0.5 V (rms, verified to be within the linear response regime) was applied. Impedance data were analyzed using the ZView software (version 3.5, Scribner Associates, Inc.) with equivalent circuit modeling to extract bulk resistance and capacitance parameters.

3. Results and discussion

3.1. Single crystal X-ray diffraction study

Single-crystal X-ray diffraction (SXRD) was used to determine the crystal structure of the hybrid compound $(CH_3NH_3)_3(SbCl_5)\cdot Cl$. Table 1 summarizes the primary crystallographic data and refinement parameters.

The compound crystallizes in the monoclinic system with the centrosymmetric space group $P2_1/n$ at 293 K. The unit cell

Table 1 Main crystallographic X-ray diffraction data parameters of the hybrid compound $(CH_6N)_3(SbCl_5)\cdot Cl$

Formula	$[(CH_6N)_3(SbCl_5)\cdot Cl]$
Formula weight	430.88
Temperature/K	298.15
Crystal system	Monoclinic
Space group	$P2_1/n$
a/Å	13.0073(2)
b/Å	8.0388(2)
c/Å	15.1149(4)
β/°	95.669(42)
Volume/Å^3	1572.73(6)
Z	4
ρ_{calc} (g cm^{-3})	1.819
μ/mm^{-1}	2.745
F(000)	840.0
Crystal size/mm^3	0.53 × 0.09 × 0.07
Data collection instrument	Kappa CCD
Radiation	Mo Kα (λ = 0.71073)
2θ range for data collection/°	5.548 to 62.928
Index ranges	$-18 \le h \le 19$, $-11 \le k \le 11$, and $-22 \le l \le 21$
Reflections collected	22 913
Independent reflections	5224
Goodness-of-fit on F^2	1.071
Final R indexes	$R_1 = 0.03$ and $wR_2 = 0.05$
Largest diff. peak/hole/e Å^{-3}	0.41/−0.61
CCDC deposition number	2443838

parameters are as follows: $a = 13.0073(2)$ Å, $b = 8.0388(2)$ Å, $c = 15.1149(4)$ Å, $\beta = 95.669(2)°$, with unit cell volume (V) = 1572.73(6) Å^3. The number of formula units per unit cell is $Z = 4$, yielding a calculated density (ρ_{calc}) of 1.819 g cm^{-3}.

The asymmetric unit of the structure, as shown in Fig. 1, contains three organic cations, $CH_3NH_3^+$(methylammonium),

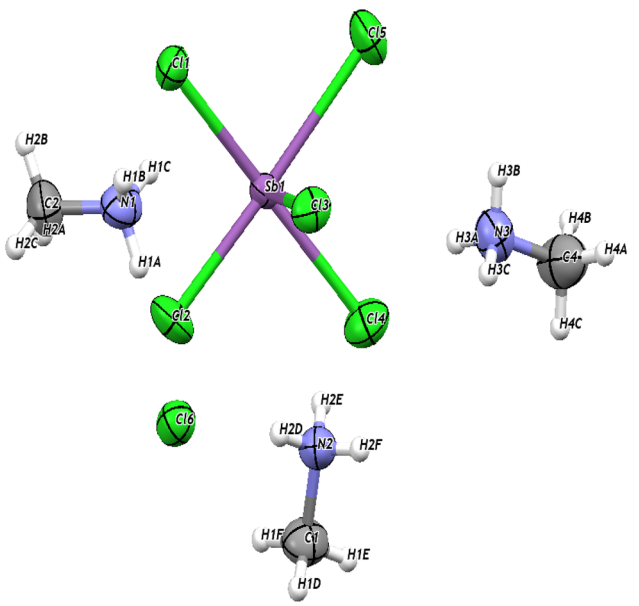

Fig. 1 Perspective view of the asymmetric unit of $(CH_3NH_3)_3(SbCl_5)\cdot Cl$ at the 50% probability ellipsoids.

one inorganic complex anion, $SbCl_5^{2-}$ (pentachloroantimonate(III)), and one additional noncoordinated chloride anion, Cl^-. These three organic $CH_3NH_3^+$ cations neutralize the overall charge of the $[SbCl_5]^{2-}$ anion and the Cl^- anion, thus ensuring the electrical neutrality of the compound.

The coordination environment of the antimony atom Sb1 is distorted bipyramidal (see Table S1). The Sb_1 atom is surrounded by five chlorine atoms (Cl_1, Cl_2, Cl_3, Cl_4, and Cl_5) forming a $[SbCl_5]^{2-}$ unit. The Sb–Cl bond lengths range from 2.4740(6) Å (Sb_1–Cl_3) to 2.6790(7) Å (Sb_1–Cl_4), indicating a notable deviation from the ideal geometry. The bond angles around Sb_1 confirm this distortion: the angle Cl_1–Sb_1–Cl_4 is nearly linear (172.56(2)°), corresponding to the bipyramidal axis, while equatorial angles (*e.g.*, Cl_3–Sb_1–Cl_2 = 91.19(2)°) are close to 90°.

The organic $CH_3NH_3^+$ cations (represented by atoms N_1, N_2, and N_3) are connected to the $[SbCl_5]^{2-}$ anion and the free Cl^- anion (Cl_6) *via* a complex network of N–H···Cl hydrogen bonds. As shown in Fig. 2 and Table 2, these interactions are numerous and varied. For example, atom N_1 forms three hydrogen bonds with Cl_6, Cl_5, and Cl_1. Similarly, atoms N_2 and N_3 form multiple bonds with different chlorine atoms. Collectively, these interactions establish a coherent three-dimensional (3D) network that contributes to the stability of the crystal structure.

As summarized in the crystallographic comparison in Table 3, the structural features of $(CH_3NH_3)_3(SbCl_5)\cdot Cl$ can be contextualized within the broader family of hybrid chloridoantimonates(III). Unlike conventional Sb–Cl hybrids, in which the anion adopts either a $[SbCl_5]^{2-}$ square-pyramidal[22] or $[SbCl_6]^{3-}$ distorted-octahedral geometry,[23] our compound exhibits a $(CH_3NH_3)_3(SbCl_5)\cdot Cl$ stoichiometry that includes a free, uncoordinated chloride ion. To the best of our knowledge, this configuration is rare within the family of hybrid chloridoantimonates(III) and has not been previously reported with the methylammonium cation. The antimony atom adopts a $[SbCl_5]^{2-}$ distorted trigonal bipyramidal geometry with characteristic Sb–Cl distances. This geometry is consistent with the presence of a stereochemically active Sb(III) lone pair; however, the crystal packing differs from that observed in $[NH_4]_2[SbCl_5]$[22] due to the nature and arrangement of the organic cations. The simultaneous presence of methylammonium cations ($CH_3NH_3^+$) and free chloride anions enables the formation of a unique three-dimensional N–H···Cl hydrogen-bond network, distinct from the 1D or 2D patterns observed in $[(CH_3)_nNH_{4-n}]_3[Sb_2Cl_9]$ (n = 2 and 3) compounds.[24] This network enhances crystal stability and may influence the dielectric or optical properties of the material.

3.2. Optical properties

3.2.1. UV-visible study. The fundamental processes of light transmission, reflection, and absorption in materials are intrinsically linked to their electronic structures. In this section, we present and analyze the compound's basic optical properties to assess its quality and optical performance.[25] UV-visible spectroscopy, which probes molecular interactions with ultraviolet and visible light, provides valuable information on the

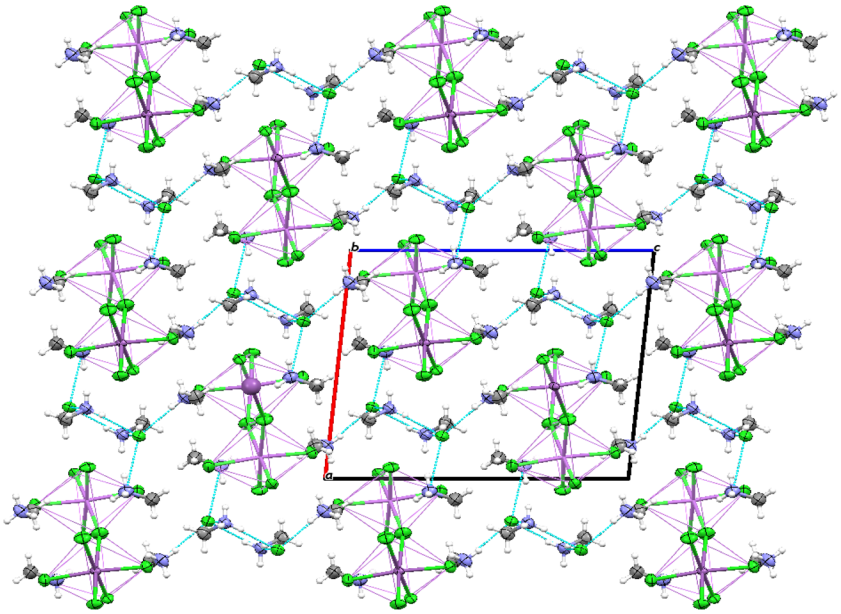

Fig. 2 Projection of the packing arrangement of the $(CH_3NH_3)_3(SbCl_5)\cdot Cl$ compound in the plane (*a*, *c*) showing its hydrogen bonds.

Table 2 Hydrogen bonds of $(CH_3NH_3)_3(SbCl_5)\cdot Cl$[a]

D—H···A	D—H (Å)	H···A (Å)	D···A (Å)	D—H···A (°)
N1–H1A···Cl6(i)	0.89	2.321(i)	3.206(i)	173.07(i)
N1–H1B···Cl5(i)	0.89	2.760(i)	3.552(i)	149.00(i)
N1–H1C···Cl1(i)	0.89	2.577(i)	3.229(i)	155.04(i)
N2–H2D···Cl6(i)	0.89	2.302(i)	3.183(i)	170.47(i)
N2–H2E···Cl3 (i)	0.89	2.870(i)	3.346(i)	115.07(i)
N2–H2E···Cl4 (i)	0.89	2.503(i)	3.348(i)	158.67(i)
N3–H3A···Cl4(i)	0.89	2.507(i)	3.349(i) (3)	157.87(i)
N1–H1B···Cl1(ii)	0.89	2.729(ii)	3.317(ii)	124.61(ii)
N2–H2F···Cl6(iii)	0.89	2.729(iii)	3.317(iii)	163.61(iii)
N3–H3C···Cl6(iv)	0.89	2.599(iv)	3.383(iv)	147.42(iv)
C4–H4B···Cl1 (v)	0.89	2.952(v)	3.89(v)	166.57(v)

[a] Symmetry codes: (i): x, y, z; (ii): $-x+1, -y+1, -z+1$; (iii): $-x+\frac{1}{2}+1, y+\frac{1}{2}, -z+\frac{1}{2}$; (iv): $x-\frac{1}{2}, -y+\frac{1}{2}+1, z-\frac{1}{2}$; and (v): $-x+\frac{1}{2}, y+\frac{1}{2}, -z+\frac{1}{2}$.

molecular characteristics, chemical structure, and electronic transitions. Fig. 3a shows the UV-vis absorption spectrum measured at room temperature for $(CH_3NH_3)_3(SbCl_5)\cdot Cl$, covering the wavelength range of 200–800 nm. The spectrum displays two well-defined absorption bands at 274 nm and 356 nm, which can be attributed to distinct electronic processes within the hybrid material. The absorption observed in the near-UV region around 274 nm is associated with high-energy electron–hole excitations localized within the $[SbCl_5]^{2-}$ anion. These excitations occur above the conduction band edge and are followed by rapid carrier relaxation, which influences both the optical response and charge transport behavior. The absorption band centered near 356 nm is assigned to a ligand-to-metal charge transfer (LMCT), involving electron transfer from chloride 3p orbitals to antimony 5p states, highlighting the strong electronic coupling within the inorganic anionic framework. Furthermore, the energy band gap arises from electronic transitions between the valence and conduction bands, and the pronounced absorption extending into the visible region indicates that this feature is intrinsic to the fundamental band structure of the material.

The optical band gap energy (E_g) can be determined using several approaches. The Tauc plot method assumes that the absorption edge results from an interband transition between parabolic bands. However, this approach is not appropriate for materials exhibiting significant band tails that overlap the fundamental absorbance or for low-dimensional (2D, 1D, or 0D) systems.[26] Because $(CH_3NH_3)_3(SbCl_5)\cdot Cl$ crystallizes in a three-dimensional framework, the Tauc formalism is suitable for estimating its optical band gap, particularly for powdered samples. The optical band gap energy (E_g) can be determined from the following relation:

Table 3 Crystallographic data and structural comparison of $(CH_3NH_3)_3(SbCl_5)\cdot Cl$ with the selected hybrid chloroantimonates(III)

Compound	Crystal system	Space group	*a* (Å)	*b* (Å)	*c* (Å)	*β* (°)	*V* (Å^3)	Ref.
$(CH_3NH_3)_3(SbCl_5)\cdot Cl$	Monoclinic	$P2_1/n$	13.0073	8.0388	15.1149	95.669	1572.73	This study
$[NH_4]_2[SbCl_5]$	Orthorhombic	*Pnma*	7.45	10.82	13.21	—	1065	22
$(C_6H_{14}N_2)_2[Sb_2Cl_{10}]\cdot H_2O$	Orthorhombic	$Pna2_1$	29.122	8.403	11.358	—	2779.4	23
$[(CH_3)_2NH_2]_3[Sb_2Cl_9]$	Monoclinic	*Pc*	9.313	9.001	14.109	95.01	1182	24
$[(CH_3)_3NH]_3[Sb_2Cl_9]$	Monoclinic	*Pc*	9.865	9.113	15.096	89.99	1356	24

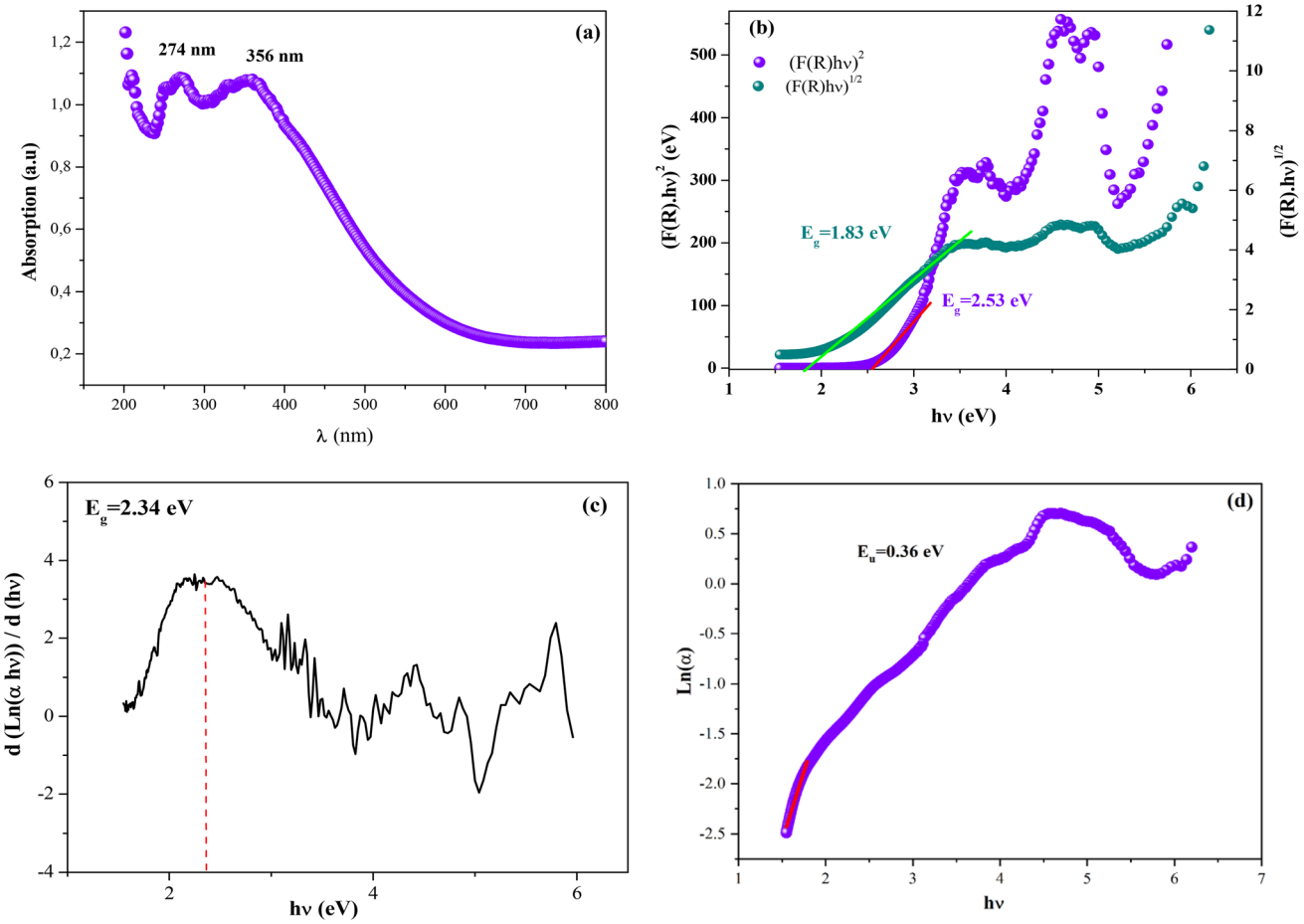

Fig. 3 (a) Absorbance spectrum, (b) dependence of $(F(R) \times h\nu)^2$ and $(F(R) \times h\nu)^{1/2}$ on the energy ($h\nu$), (c) their first derivative on the energy ($h\nu$), and (d) ln (α) as a function of $h\nu$ for the $(CH_3NH_3)_3(SbCl_5)\cdot Cl$ compound.

$$(\alpha h\nu)^{1/n} = B\,(h\nu - E_g), \tag{1}$$

where the Kubelka–Munk function, $F(R)$ is defined by the following expression:[27]

$$F(R) = (1 - R)^2/2R. \tag{2}$$

Here, R denotes the diffuse reflectance. In the Tauc relation, B is an energy-independent constant associated with band tailing effects, α corresponds to the optical absorption coefficient, and $h\nu$ represents the photon energy (in eV). The parameter E_g refers to the optical band gap energy, while n characterizes the nature of the electronic transition between the valence and conduction bands.[28,29] Specifically, $n = 1/2$ corresponds to direct allowed transitions, $n = 2$ to indirect allowed transitions, $n = 3/2$ to direct forbidden transitions, and $n = 3$ to indirect forbidden transitions. It should be noted that the Kubelka–Munk approach, derived from reflectance measurements, is commonly applied to opaque materials. Within this framework, the absorption coefficient can be approximated as $\alpha \approx F(R)/e$, where e is the sample thickness. In fact, we have presented the curve of $(F(R)\ h\nu)^{1/n}$ as a function of the photon's energy ($h\nu$) for $n = 2$ and $n = 1/2$ in Fig. 3b. The direct and indirect optical band gaps were found by extending these plots, and the intersection of the fitted straight line with the $(F(R)\ h\nu)^{1/n}$ axis ($y = 0$) was used to get the E_g value of our sample. As a result, the band gap is discovered to be 2.53 eV for $n = 0.5$ and 1.83 eV for $n = 2$.

In contrast, to verify the value of the gap energy for the studied sample, we used the first-order derivative of the Tauc equation and its natural logarithm to obtain eqn (3) and (4) as follows:

$$\ln(\alpha h\nu) = n \quad \ln \quad B + n \quad \ln(h\nu - E_g), \tag{3}$$

$$\frac{\mathrm{d}\ \ln(\alpha h\nu)}{\mathrm{d}(h\nu)} = n\left(\frac{1}{h\nu - E_g}\right). \tag{4}$$

Eqn (4) states that the curve of $\mathrm{d}(\ln(\alpha h\nu)/\mathrm{d}(h\nu))$ against $h\nu$ should have a peak at the location where $E_g = h\nu$. For the sample $(CH_3NH_3)_3(SbCl_5)\cdot Cl$, the plot of $\mathrm{d}(\ln(\alpha h\nu)/\mathrm{d}(h\nu))$ against $h\nu$ is displayed in Fig. 3c. The abscissa's peak at a specific energy value gives the approximate value of E_g. The estimated band gap is found to be 2.34 eV. Furthermore, the reflectance results are in good agreement with both the band gap value and the direct nature of the electronic transition reported for a previously studied organic–inorganic hybrid compound, namely

$(C_8H_{14}N_2)(SbCl_5)$.[30] Therefore, $(CH_3NH_3)_3(SbCl_5)\cdot Cl$ is a potential candidate for fundamental optoelectronic studies. The band tail energy, commonly referred to as the Urbach energy, represents the extent of localized electronic states near the conduction band edge. It provides insight into stoichiometric defects that arise from the incorporation and interaction of magnetic ions within the material. From a physical standpoint, the Urbach tail offers a qualitative insight into the crystallinity of a material and reveals the presence of imperfections such as defects, disorder, and impurities. It serves as an effective measure of short-range structural order and indicates the existence of localized defect states in disordered semiconductors, thereby providing important information about the material's electronic structure and overall degree of disorder.

The Urbach tail energy (E_u) can be experimentally evaluated by applying the Urbach–Martienssen relation, as described below:[31]

$$\alpha = \alpha_0 \exp\left(\frac{h\nu - E_g}{E_u}\right), \quad (5)$$

$$\ln \alpha = \ln \alpha_0 + \frac{h\nu - E_g}{E_u}. \quad (6)$$

In this equation, α_0 is a constant, E_u represents the Urbach energy (in electron volts, eV), and $h\nu$ denotes the photon energy, also expressed in electron volts (eV). The fluctuation of ln (α) *vs.* ($h\nu - E_g$) is shown in Fig. 3d using eqn (6). A linear fit of the low-energy absorption edge yields a slope of approximately 2.77, from which the Urbach energy is calculated as E_u = 1/slope = 0.36 eV. This relatively high Urbach energy indicates the presence of structural defects and a significant degree of disorder within the material.

The optical properties of a material are governed by the interaction between matter and the electric field of an incident electromagnetic wave. The absorption of electromagnetic radiation depends on several factors, including the material thickness, refractive index (n), photoconductivity, and extinction coefficient (K). According to established principles, the attenuation of incident electromagnetic radiation within a sample is related to its crystalline arrangement and surface morphology. Specifically, the amplitude of the electromagnetic wave decreases by a factor of 1/e after propagating through a distance equal to the penetration depth. The penetration depth (δ), also referred to as the absorption depth in optical contexts, can be calculated using the following expression: $\delta = 1/\alpha$.

Typically, this value ranges from a few hundred to several thousand ångströms (Å), depending on the material and its synthesis method. The propagation of an electromagnetic wave through the compound can be described using the complex refractive index (N), which is frequency-dependent as follows:

$$N = n - iK, \quad (7)$$

where n is the real part of the refractive index, related to the phase velocity of light in the material, and k is the extinction coefficient. The extinction coefficient (Fig. 4) quantifies the exponential decay of the electromagnetic wave amplitude within the material. Specifically, the absorption coefficient (α) and extinction coefficient (k) are related by the following equation:[32]

$$K(\lambda) = \frac{\alpha(\lambda)\lambda}{4\pi}. \quad (8)$$

Indeed, when the photon energy ($h\nu$) increases, a notable decrease in the penetration depth (δ) is seen (Fig. 4). This degradation may be attributed to the attenuation of the incoming photon energy near the surface under light exposure, likely resulting from structural deformation within the crystal. Additionally, the transparency region of the compound is characterized by the remaining extinction coefficient (k) values.[33] However, the $(CH_3NH_3)_3(SbCl_5)\cdot Cl$ compound transmits almost all of the incident energy due to its total transparency in the visible band (Fig. 4). Due to their low visible-range attenuation coefficient, the crystals can be used in

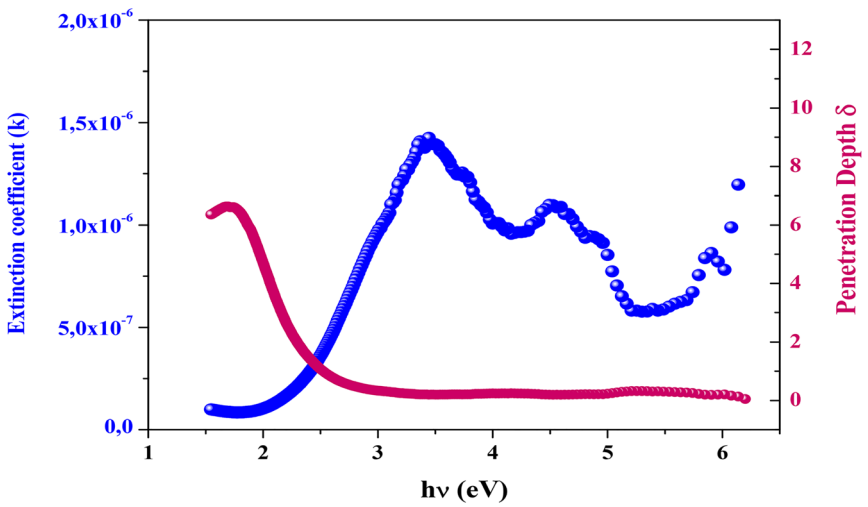

Fig. 4 Extinction coefficient and penetration depth (δ) plots of the $(CH_3NH_3)_3(SbCl_5)\cdot Cl$ compound.

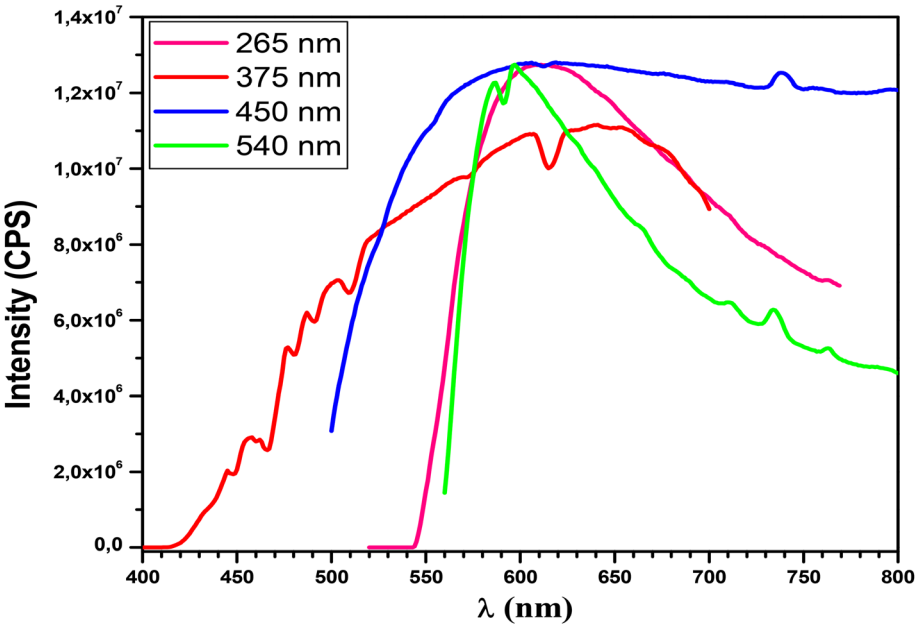

Fig. 5 PL spectra of the $(CH_3NH_3)_3(SbCl_5)\cdot Cl$ compound at four distinct excitation wavelengths (265, 375, 450 and 540 nm).

nonlinear optical applications and as antireflection layers in solar thermal systems.[34]

3.2.2. Photoluminescence study. Fig. 5 displays the photoluminescence (PL) emission spectra of $(CH_3NH_3)_3(SbCl_5)\cdot Cl$ recorded at four distinct excitation wavelengths (265, 375, 450, and 540 nm). The emission band is asymmetrically broadened toward longer wavelengths and peaks at approximately 600–610 nm, independent of the excitation wavelength. This spectral invariance strongly suggests that the emission originates from a single emissive state, commonly attributed to self-trapped excitons (STEs).[35]

The intensity of the PL signal varies according to the excitation wavelength: it is maximum under an excitation of 450 nm, decreases significantly at 540 nm and has intermediate values for excitations at 265 and 375 nm. This variation directly mirrors the compound's absorption profile, which exhibits stronger absorption in the blue region (450 nm) compared to the red region (about 540 nm). Consequently, excitation at 450 nm generates a higher density of photoexcited carriers capable of populating the emissive state (likely an STE), thereby yielding enhanced PL intensity.[36]

The optimal excitation wavelength (450 nm) produces an emission centered at approximately 600 nm, corresponding to a Stokes shift of about 150 nm. This substantial Stokes shift is characteristic of STE systems and arises from structural relaxation upon photoexcitation.[37]

The broad (full width at half-maximum (FWHM) = 100–150 nm) and highly asymmetric PL peak is consistent with the phonon-assisted radiative recombination of STEs, a hallmark of materials exhibiting strong electron–phonon coupling.[37] The assignment of the observed broadband emission to self-trapped excitons (STE) is further reinforced by the intrinsic structural and electronic landscape of $(CH_3NH_3)_3(SbCl_5)\cdot Cl$. The stereochemically active Sb^{3+} $5s^2$ lone pair drives a pronounced distortion of the $[SbCl_5]^{2-}$ polyhedron, which, together with the rigid three-dimensional N–H···Cl hydrogen-bonding framework, creates a locally compliant lattice environment highly favorable for exciton self-trapping. This structural predisposition is consistent with the relatively high Urbach energy (0.36 eV), indicative of substantial lattice disorder and shallow localized states that promote carrier confinement. Within the family of Sb(III)- and Bi(III)-based hybrid halides, the concurrent presence of excitation-independent broad emission, a large Stokes shift, and a distorted inorganic sublattice has been widely adopted as a reliable fingerprint for STE recombination, even in initial reports lacking time-resolved or temperature-dependent photoluminescence data.[38–40]

3.3. Electrical properties

3.3.1. Nyquist diagram and equivalent circuit. Complex impedance spectroscopy (CIS) is a valuable technique for characterizing the electrical activity of $(CH_3NH_3)_3(SbCl_5)\cdot Cl$. CIS analyzes the material's impedance response to reveal information about ion transport inside the lattice as well as the material's general electrical conductivity.[41] This technique demonstrates a direct correlation between the response of the real system and the equivalent circuit formed by the electrical components. This technique is a potent, nondestructive method for examining a material's electrical characteristics. Unlike other methods, CIS does not damage samples while providing vital information about important parameters like the electrical conductivity, relaxation time, and ion mobility within the $(CH_3NH_3)_3(SbCl_5)\cdot Cl$ perovskite. Additionally, one of CIS's key advantages is its capacity to distinguish between contributions from different sources within the material. Charge carriers are set in motion when an alternating electric

field is applied, which induces processes such as space charge polarization, dipole reorientation, and charge displacement. Through this dynamic process, sophisticated impedance analysis can efficiently identify the specific functions that electrodes, grains, and grain boundaries play in facilitating charge transport through the material.

Fig. 6 displays a Nyquist plot of the complex impedance of the $(CH_3NH_3)_3(SbCl_5)\cdot Cl$ specimen recorded over the temperature range of 313–363 K. The depressed centers of the semicircles, located below the real axis, indicate non-Debye characteristics. This finding demonstrates that conduction in $(CH_3NH_3)_3(SbCl_5)\cdot Cl$ adheres to the Cole–Cole formalism, which implies a relaxation time distribution. The distribution of relaxation times resulting from inhomogeneities, such as grain boundary effects, defects, and microstructural disorder, is indicated by this depression and deviation from the ideal Debye behavior. A typical frequency dependence is observed in the Nyquist plots, where the frequency is lowest at the high Z' end (right side) and increases toward the origin (left side), peaking at the intersection with the imaginary axis. The material's capacitive properties are further supported by this frequency response. The impedance spectra exhibit two separate semicircles, each of which represents a particular frequency domain. Furthermore, the geometry of the spectra shows two separate semicircles, each of which represents a particular frequency domain. The grain boundary contribution is responsible for the low-frequency semicircle, whereas the bulk grain response is responsible for the high-frequency semicircle. More specifically, the resistance values derived from the fitting procedure can be used to differentiate between the two contributions. The grain boundary effect is linked to the arc exhibiting greater resistance, whereas the grain effect is related to the arc with lower resistance. The greater arc dispersion at low frequencies suggests that the grain boundary is more resistive. Further proof that the material exhibits a negative temperature coefficient of resistance (NTCR) is provided by the fact that the radius of the semicircle in the Cole–Cole diagram decreases as the temperature rises.[42] This observed trend indicates an improvement in charge carrier mobility. It can be explained by improved hopping mechanisms or interstitial diffusion within the grains, as well as the reduction of electrostatic potential barriers at grain boundaries. The temperature-dependent response is characteristic of the semiconducting behavior of $(CH_3NH_3)_3(SbCl_5)\cdot Cl$, in which the electrical conductivity is governed by the thermal activation of ionic species (such as organic cation motion) and electronic charge carriers (electrons or holes) associated with antimony-related states.[43] It should be emphasized that the electrical and dielectric spectroscopy measurements presented here are aimed at elucidating the fundamental mechanisms underlying the charge transport and relaxation phenomena in $(CH_3NH_3)_3(SbCl_5)\cdot Cl$ rather than replicating the specific operating conditions of practical electrochemical energy storage or device applications.

The theoretical curves (lines) and experimental data are in excellent agreement, as shown in Fig. 6. This alignment verifies that the electrical characteristics of the sample are appropriately represented by the selected equivalent circuit.

Notably, the best fit is obtained using an equivalent electrical circuit consisting of a resistance (R_1) in parallel with a constant phase element (CPE_1) and a capacitance (C_1) to model the grain response in series with a resistance (R_2) in parallel with a constant phase element (CPE_2) to describe the grain boundary (inset of Fig. 6). The interpretation that the total electrical response is considerably influenced by both grain and grain boundary effects is validated by the excellent match between experimental data and this circuit model. The circuit was really chosen because of its low fitting errors and good agreement with the experimental results.

The existence of multiple relaxation processes that exhibit roughly identical or comparable relaxation times in the $(CH_3NH_3)_3(SbCl_5)\cdot Cl$ system may lead to nonideal capacitance behavior, which is accounted for by the constant phase element

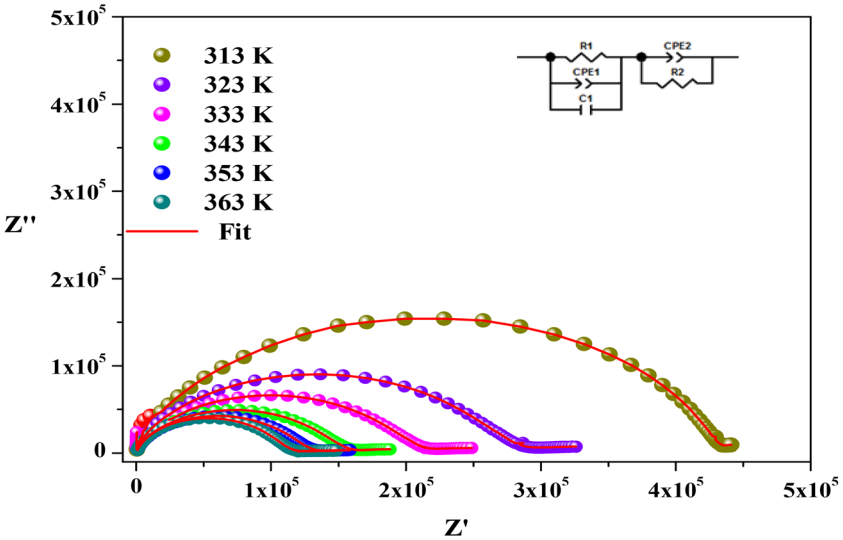

Fig. 6 Nyquist plots of the complex impedance of $(CH_3NH_3)_3(SbCl_5)\cdot Cl$ at various temperatures and theoretical data (solid line) (inset: electrical equivalent circuit).

Table 4 Electrical values of the equivalent circuit parameters calculated for the $(CH_3NH_3)_3(SbCl_5)\cdot Cl$ compound at different temperatures

T (K)	R_1 (10^5 ω)	C_1 (10^{-10} F)	Q_1 (10^{-8} F)	α_1	R_2 (10^5 ω)	Q_2 (10^{-10} F)	α_2
313	2.45(1)	0.80(1)	1.77(1)	0.39(3)	4.17(2)	3.03(8)	0.90(2)
323	1.78(1)	1.27(1)	5.14(5)	0.41(3)	2.96(1)	3.49(3)	0.88(2)
333	1.13(1)	1.15(1)	4.56(4)	0.44(3)	2.07(1)	4.12(3)	0.81(3)
343	0.65(1)	1.06(1)	2.21(2)	0.48(3)	1.27(7)	9.03(7)	0.83(3)
353	0.43(1)	1.51(1)	3.85(3)	0.45(3)	0.88(4)	6.62(5)	0.84(2)
363	0.34(1)	1.99(1)	7.68(7)	0.40(3)	0.63(3)	4.02(3)	0.87 ± 0.02

(CPE) in the corresponding circuit models. The following kind of empirical function is used to calculate the impedance contribution of the CPE:

$$Z_{\text{cpe}} = \frac{1}{Q \times (j\omega)^{\alpha}}, \tag{9}$$

where the imaginary unit is denoted by j ($j^2 = -1$), Q is the CPE pre-exponential factor, ω denotes the angular frequency ($\omega = 2\pi f$, where f is the frequency), and α is a dimensionless parameter ranging between 0 and 1. The exponent α determines the phase angle, $\beta = \alpha\pi/2$, which represents the angle between the radius of the semicircle and the Z' axis in Nyquist coordinates. When $\alpha = 1$, the CPE behaves as an ideal capacitor, and the constant Q equals the capacitance C.[44] Bhomik *et al.* demonstrated that the presence of a constant phase element (CPE) with $\alpha < 1$ indicates non-Debye-type dielectric relaxation.[45] This behavior is usually linked to structural or compositional heterogeneities in the material, as well as a distribution of relaxation times associated with parallel R–C elements. Conversely, when $\alpha = 0$, the CPE behaves as a perfect resistor.[46]

In fact, Table 4 summarizes the parameter values extracted from the equivalent circuit analysis for modeling the electrical response, arranged by temperature. The CPE parameter Q_2 exhibits values around 10^{-10} F, while Q_1 is on the order of 10^{-8} F. This difference suggests that the bulk grain response is represented by the first equivalent circuit branch and the grain boundary response by the second branch. Furthermore, as Table 4 illustrates, R_2 (grain boundary resistance) values are consistently greater than R_1 (grain resistance) values at all temperatures. This demonstrates the significant contribution of grain boundaries to the total resistance. In general, grain growth at high temperatures is often attributed to enhanced atomic mobility and reduced disorder at grain boundaries. As a result, both grain and grain boundary resistances decrease with increasing temperature, which is consistent with the semiconducting characteristics of the material.

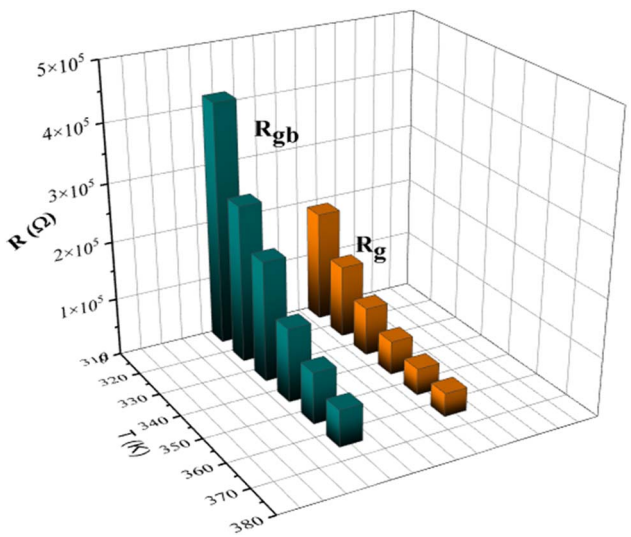

Fig. 7 Variation in the strength of the grains and grain boundaries of the $(CH_3NH_3)_3(SbCl_5)\cdot Cl$ compound.

In fact, Fig. 7 shows the temperature dependence of grain and grain-boundary resistance.

The previously described negative temperature coefficient of resistance (NTCR) behavior is confirmed by the clear decrease in both grain and grain boundary resistances as the temperature increases. This trend is supported by the detected reduction in both grain and grain boundary resistances as the temperature rises. Such a behavior can be explained by several contributing factors, including variations in the grain boundary structure, the influence of the grain size, the thermal resistance and conductance associated with tilt grain boundaries, and microscale observations of modified thermal conductivity.[47]

In this context, the reduced resistance in the grain area implies that interfaces or flaws do not hinder charge carriers at the grain borders, but rather, they can move more easily through the bulk material (grains).

3.3.2. DC conductivity. A key component of the conduction process in semiconductors is temperature-dependent DC conductivity. Under an applied electric field, the thermally activated motion of delocalized charge carriers is necessary for thermally activated electrical conductivity.

The following formula can be used to calculate the grain's electrical conductivity (σ_g) at any temperature, based on the resistance values extracted from the equivalent circuit:

$$\sigma_g = \frac{e}{R_1 S}, \tag{10}$$

where e is the sample thickness and S is the electrode area.

To analyze the conduction mechanisms and identify the activation energies, we examined the temperature dependence of the grain conductivity of $(CH_3NH_3)_3(SbCl_5)\cdot Cl$ by plotting $\ln(\sigma_g)$ *versus* $1000/T$ under a constant applied voltage of 1 V over the temperature range of 313–363 K (Fig. 8). For $(CH_3NH_3)_3(SbCl_5)\cdot Cl$, the linear behavior of the $\ln(\sigma_g T)$ *versus* $1000/T$ plot

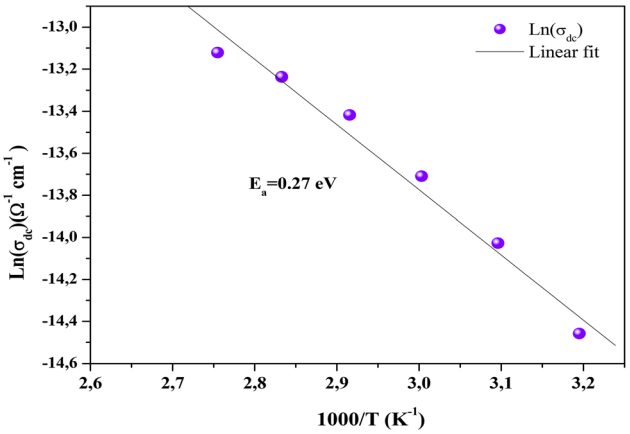

Fig. 8 Arrhenius plots for the bulk conductivity of the $(CH_3NH_3)_3(SbCl_5)\cdot Cl$ sample.

indicates that no phase transition occurs within the studied temperature interval. As evidenced by the plot, the DC conductivity increases exponentially with temperature, revealing a thermally activated transport mechanism. The temperature rise provides additional thermal energy, which enhances the population of mobile charge carriers. This characteristic is consistent with an Arrhenius-type conduction model and is typical of thermally assisted hopping or tunneling between localized energy levels,[48] as follows:

$$\sigma_g = \sigma_0 \exp\left(-\frac{E_a}{K_B T}\right), \quad (11)$$

where K_β represents the Boltzmann constant, σ_0 denotes the pre-exponential factor related to the density of states and charge carrier mobility, T is the absolute temperature, and E_a denotes the activation energy for grain conductivity. Based on a linear fit to the data points, the activation energy derived from Arrhenius law is calculated to be around $E_a = 0.27$ eV.

3.3.3. AC conductivity. The thermally stimulated mobility of charge carriers—which undergo a hopping process when exposed to an electric field—is the primary source of electrical conductivity in disordered solids. Defect centers in disordered systems play a crucial role in this conduction process, making conductivity measurements an effective tool for investigating them. Electrical conductivity provides a highly effective macroscopic probe of microscopic charge carrier dynamics.

This technique facilitates the separation of localized and long-range conduction behaviors, thereby revealing deeper insights into the underlying relaxation mechanisms. The AC conductivity can be characterized using the following relationship:

$$\sigma'_{AC}(\omega, T) = \frac{e}{S} \times \frac{Z'}{\left(Z'^2 + Z''^2\right)}, \quad (12)$$

where Z' and Z'' are the real and imaginary components of the complex impedance, respectively, and e and S represent the sample thickness and cross-sectional area, respectively. Fig. 9a shows the material's measured AC conductivity (σ_{ac}) over a broad range of temperatures (313–363 K) and frequencies (0.1 Hz–1 MHz). The experimental data were analyzed using Jonscher's universal power law[49] as follows:

$$\sigma_{ac} = \sigma_{dc} + A \times \omega^S, \quad (13)$$

where σ_{dc} denotes the conductivity of direct current. It is derived from the long-range translational motion of charge species by extending the low-frequency area to zero frequency.

The dispersion behavior in conductivity, which reflects the frequency dependence of the AC conductivity, is explained by the term $A\omega^S$. The temperature-sensitive coefficient, denoted by A, measures the degree of polarization resulting from the diffusive motion of charge carriers. Conversely, s is a characteristic that establishes the connection between the carriers and the medium they move across. The s exponent has a range of 0 to 1, where a value of 1 indicates that the lattice and charge carriers are not interacting. The interaction between the crystal structure and mobile ions increases as s drops from 1. As the temperature rises for this behavior, the charge species that have collected at grain boundaries have sufficient energy to cross the barrier. The jump relaxation model (JRM) proposed by Funke provides a convincing explanation for the tendencies that have been noticed. The model indicates that ions in the material can effectively hop to nearby locations at low frequencies. The first term of the Jonscher equation represents the sustained DC conductivity seen at low frequencies that eventually results from these successful hops, which also contribute to the ions' long-range translational motion. By contrast, both successful and failed hops take place in the high-frequency band. If a hop is unsuccessful, the excited ion may fluctuate before going back to where it started. This ineffective hop has no effect on conductivity because it does not contribute to the total mobility of the ion. Nonetheless, when hopping is successful, the leaping ion moves to a new location and becomes stable there, while the nearby ions relax in tandem with the stationary ion. In fact, effective hopping involves agitated leaping. The percentage of successful hops in comparison to failed ones increases in the high-frequency domain. The second part of the Jonscher equation describes the observed dispersion in the conductivity curves at high frequencies as a result of this imbalance.

Indeed, this power-law equation (eqn (13)) can be described by the Almond relation as follows:

$$\sigma_{ac} = \sigma_{dc}\left(1 + \left(\frac{\omega}{\omega_h}\right)^s\right), \quad (14)$$

where ω_h denotes the characteristic "hopping frequency" of the charge carriers. This parameter represents the frequency at which the dispersion region begins to emerge, marking the transition from DC to AC behavior. Notably, ω_h shifts toward higher frequencies as the temperature increases, suggesting thermally activated hopping. The following relationship might be used to express it:

$$\omega_h = \left(\frac{\sigma_{dc}}{A}\right)^{1/S}. \quad (15)$$

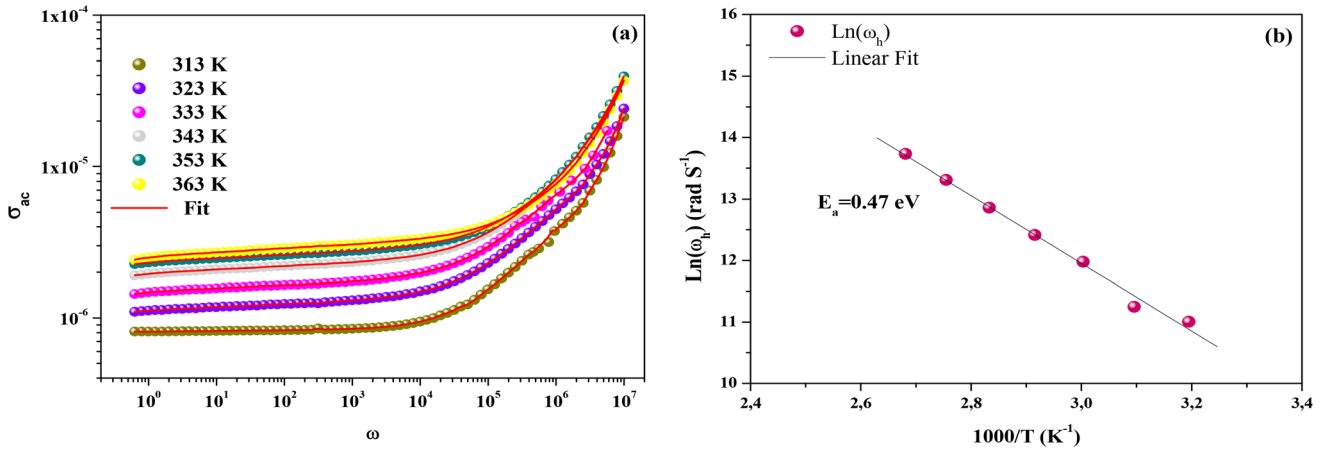

Fig. 9 (a) Frequency dependence of alternating current conductivity at several temperatures. (b) Plot of the hopping frequency ω_h *versus* the inverse of temperature.

A plot of $\ln(\omega_h)$ *versus* $1000/T$ for grain conduction is displayed in Fig. 9b. The continuous slope of the curve indicates that the compound does not undergo a phase transition within the studied temperature range. According to a linear fit of the data, the activation energy for this dynamic process, which exhibits Arrhenius-type behavior, is approximately $E_a = 0.47$ eV. This value differs from the activation energy derived from the grains' DC conductivity (σ_g), suggesting that the mobility of charge carriers in the studied compound is not governed solely by a simple hopping mechanism.

To evaluate this hypothesis, the temperature dependence of the exponent s was analyzed, offering a valuable insight into the fundamental characteristics of the conduction pathways.

The charge transfer mechanism in $(CH_3NH_3)_3(SbCl_5)\cdot Cl$ can be investigated by examining several theoretical models based on the temperature dependence of the exponent s (T). These models describe the correlation between the AC conductivity and s (T), as well as their respective dependencies on the temperature and frequency in disordered materials.

The literature presents several theoretical models that are suitable for interpreting the present results, including Long's overlapping large polaron tunneling (OLPT) model,[50] the quantum mechanical tunneling (QMT) model introduced by Austin-Mott,[51] the correlated barrier hopping (CBH) model proposed by Elliott,[52] and the nonoverlapping small polaron tunneling (NSPT) model also proposed by Austin-Mott.[51] These models are based on quantum mechanical tunneling, the thermally activated hopping of charge carriers over potential barriers, or a combination of both processes. In addition, several theoretical approaches have been proposed to characterize the nature of charge carriers, which are frequently described as polarons—quasiparticles formed by the coupling of charge carriers with lattice distortions.

According to the Austin-Mott theory,[51] the conduction mechanisms in $(CH_3NH_3)_3(SbCl_5)\cdot Cl$ can be determined by analyzing the variation of the exponent s, which reflects the interaction between mobile ions and their surroundings. Accordingly, the variation of the exponent S with temperature for our sample is shown in Fig. 10. Our experimental data demonstrate a steady increase in s with increasing temperature, which is typical of the NSPT model and indicates the predominance of small polaron hopping processes within the compound, as will be explained later. Specifically, localized charge carriers interact with the lattice to form polarons, which can hop between neighboring sites. During this process, a polaron may either return to its original position (a failed hop) or become stabilized at a new location (a successful hop) as the system seeks a lower-energy configuration. The formation of polarons arises from the coupling between charge carriers and lattice distortions as they propagate through the material. At low frequencies, successful polaron hopping is responsible for the frequency-independent (plateau) behavior of AC conductivity, as polarons effectively migrate from one site to another.[53]

In contrast, when the frequency increases, a higher proportion of unsuccessful hopping events occurs, which leads to a shift toward dispersive conductivity. Polaron formation in the majority of inorganic halide perovskites is believed to result from lattice distortions, which are not explicitly considered in

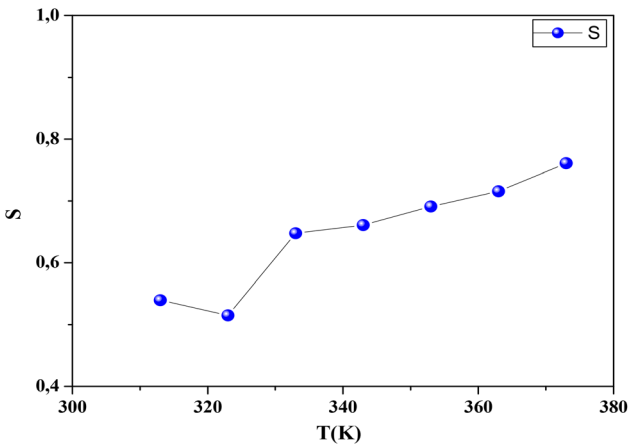

Fig. 10 Variation in the universal exponent s as a function of the temperature for $(CH_3NH_3)_3(SbCl_5)\cdot Cl$.

quantum mechanical tunneling models. In $(CH_3NH_3)_3(SbCl_5)\cdot Cl$, small polarons form when a charge carrier is localized at a particular site, causing significant local lattice deformation. Because the polarons remain spatially confined, these distortions remain localized, preventing overlap. At higher temperatures, AC conductivity can be attributed to charge carrier trapping at structural defects or to polaron tunneling processes.

The low activation energy ($E_a = 0.27$ eV), combined with the fitting of the AC conductivity data to the NSPT (nonoverlapping small polaron tunneling) model and the strong electron–phonon interaction demonstrated by photoluminescence, indicates that the dominant conduction mechanism in $(CH_3NH_3)_3(SbCl_5)\cdot Cl$ is electronic, *via* the jumping of small polarons located at antimony sites. Although the dynamics of $CH_3NH_3^+$ cations and the presence of N–H···Cl bonds may contribute to dielectric relaxation phenomena, the long-distance migration of ionic species (Cl^- or protons) is made unlikely by the rigidity of the $[SbCl_5]^{2-}$ lattice and the strength of hydrogen interactions.

3.4. Modulus study

A thorough examination of the complex modulus spectra was carried out to gain insights into the relaxation mechanisms in $(CH_3NH_3)_3(SbCl_5)\cdot Cl$. The complex electric modulus, defined as the reciprocal of the complex permittivity, was first proposed by Macedo *et al.*[54] The electric modulus formalism is a powerful approach for investigating electrical responses within materials and for analyzing relaxation phenomena related to space charge effects, especially when long-range charge carrier motion plays a significant role. One of the main advantages of this method is its ability to suppress the impact of electrode polarization, thereby enabling a more focused examination of relaxation processes related to ionic conduction. The electric modulus describes the relaxation of the electric field within the material under conditions of constant electric displacement. It can be expressed mathematically as follows:

Table 5 Estimated values of the parameters M'', β, and ω found by the fitting of $M''(\omega)$ with the modified KWW function

T (K)	M''	β	ω
313	0.0020	0.475	120 506.465
323	0.00201	0.457	223 274.627
333	0.0019	0.327	466 496.712
343	0.00182	0.351	517 114.502
353	0.00185	0.424	445 354.626
363	0.00199	0.489	399 812.306

$$M^* = j\omega C_0 Z^* = M' + jM'' = M_\infty \left[1 - \int_0^\infty e^{-j\omega t}\left(-\frac{d\varphi(t)}{dt}\right)dt\right]. \quad (16)$$

As illustrated in Fig. 11, the $M''(\omega)$ spectra recorded at various temperatures show no discernible peak in the low-frequency region; however, a prominent, broad peak emerges at high frequencies. In the low-frequency region, charge carriers exhibit enhanced mobility, allowing them to travel over longer distances *via* successful hopping between adjacent sites. In contrast, at higher frequencies, carrier mobility becomes increasingly restricted. The emergence of these peaks provides important information about the transition of charge carriers from long-range to short-range (localized) mobility. With increasing temperature, the relaxation peaks shift toward higher frequencies, indicating a thermally activated relaxation process associated with charge carrier hopping. This behavior can be explained by the hopping dynamics of the charge carriers. This trend demonstrates a clear relationship between the temperature and ionic mobility. Furthermore, it can be inferred that thermal energy drives and governs this process. Charge carriers acquire energy through thermal activation, which enables them to hop more frequently. This increases the relaxation frequency by reducing the relaxation time. Consequently, the relaxation peaks

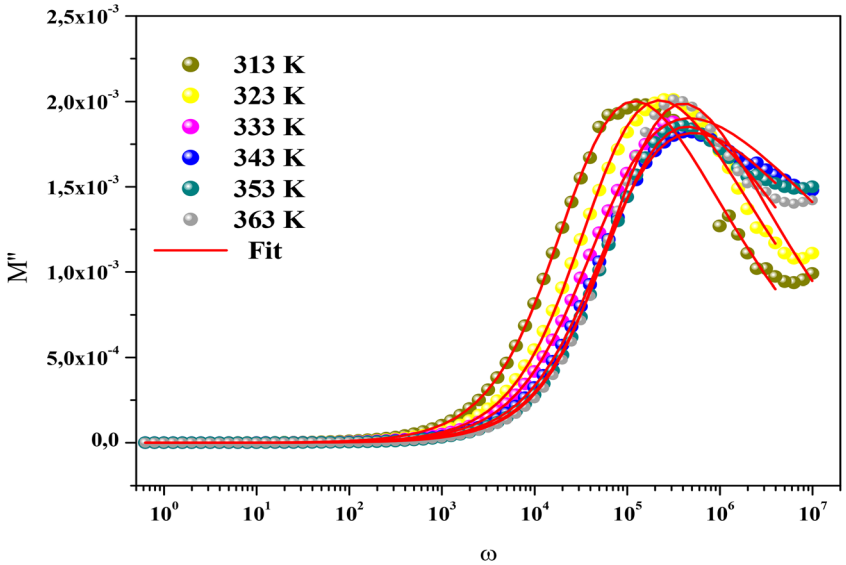

Fig. 11 Imaginary parts of the electric modulus as a function of the frequency at different temperatures for $(CH_3NH_3)_3(SbCl_5)\cdot Cl$.

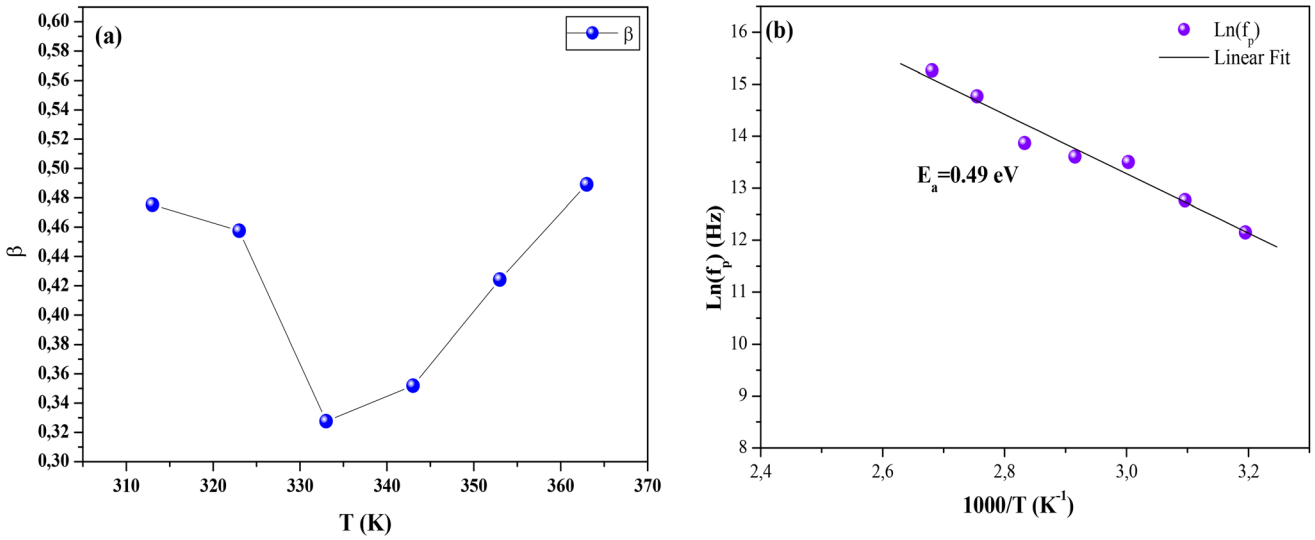

Fig. 12 (a) Temperature dependence of the b values as an Arrhenius plot for the conductivity of the $(CH_3NH_3)_3(SbCl_5)\cdot Cl$ sample. (b) Temperature dependence of the relaxation frequency (fp) for the grains of $(CH_3NH_3)_3(SbCl_5)\cdot Cl$.

shift to higher frequencies at elevated temperatures. Based on their hopping dynamics, this temperature-dependent behavior implies that the thermal activation of charge carriers influences the relaxation mechanism.[55]

The overall characteristics of the modulus spectrum provide strong evidence for a hopping mechanism, which is essential for electrical conduction within the material. Additionally, the values of the imaginary component approach zero at lower frequencies, suggesting that the modulus representation effectively suppresses electrode polarization effects. The pronounced asymmetry and broadening of these peaks indicate a wide distribution of relaxation times, each corresponding to distinct time constants. This behavior underscores the non-Debye nature of the sample's response and is consistent with observations for other related compounds.

To quantitatively describe this relaxation, the $M''(\omega)$ data were fitted using the Kohlrausch–Williams–Watts (KWW)[56] stretched exponential function, which characterizes relaxation dynamics through a stretching parameter, β, ranging from 0 to 1. Further analysis using Bergman's equation confirmed these observations as follows:

$$M'' = \frac{M''_{max}}{\left((1-\beta)+\left(\frac{\beta}{1+\beta}\right)\right)\left[\beta\left(\frac{\omega_{max}}{\omega}\right)+\left(\frac{\omega}{\omega_{max}}\right)^{\beta}\right]}. \quad (17)$$

Here, M''_{max} represents the maximum value of M'', and ω_{max} denotes the frequency at which this maximum occurs. The stretching exponent β provides a quantitative measure of the asymmetry and broadening of the loss peak. Specifically, β ranges between 0 and 1. $\beta = 1$ corresponds to ideal dipole–dipole interactions characteristic of Debye relaxation, whereas $\beta < 1$ indicates nonideal interactions associated with non-Debye behavior. Thus, the parameter β quantifies the deviation between the electrical relaxation behavior of a real solid electrolyte and that of an ideal Debye-type system. The close agreement between the experimental and theoretical curves confirms that the applied model accurately describes the M'' peak characteristics. The corresponding parameter values are provided in Table 5. The results indicate that β increases with the temperature, suggesting that $M''(\omega)$ progressively approaches ideal Debye-type behavior at higher temperatures. Notably, as previously mentioned, these results are consistent with conclusions drawn from the DC conductivity analysis.

The temperature dependence of β is illustrated in Fig. 12a. The increase in β with the temperature reflects an enhancement in the ionic and electronic transport properties of the material. This behavior is likely associated with the enhanced mobility of $(CH_3NH_3)^+$ ions within the crystal structure. At elevated temperatures, thermal energy facilitates ion diffusion across interstitial sites in the crystal lattice, thereby reducing energy barriers. This increase in ionic mobility, potentially accompanied by improved electronic conductivity, positively influences the material's electrochemical performance, which is crucial for energy storage applications. The relaxation frequencies (f_p) can be determined from the peak frequency (ω_{max}), which corresponds to the transition between long-range and short-range ionic mobility. This critical transition is governed by the relation $\omega_m \times \tau_m = 1 = 2\pi f_p$, where τ_m denotes the most probable relaxation time of the ions. The activation energy can be extracted from the plot of $\ln(f_p)$ *versus* $1000/T$, as shown in Fig. 12b. The activation energy obtained in this investigation is 0.49 eV. This result demonstrates that the relaxation dynamics are thermally activated and governed by the same energy barrier as the conduction process, which is primarily driven by the motion of thermally activated $(CH_3NH_3)^+$ cations.

4. Conclusion

The organo–inorganic hybrid compound $(CH_3NH_3)_3(SbCl_5)\cdot Cl$ was successfully synthesized using a solution-based slow

evaporation method. Single-crystal X-ray diffraction analysis revealed that the material crystallized in the monoclinic system, space group $P2_1/m$, with a three-dimensional architecture stabilized by an extensive network of N–H···Cl hydrogen bonds. Optical measurements confirmed the material's semiconducting nature and its potential for optoelectronic applications, revealing a direct band gap of 2.34 eV.

Photoluminescence analysis revealed a broad, asymmetric emission centered around 600–610 nm, regardless of the excitation wavelength, strongly suggesting an origin associated with self-trapped excitons (STEs). The substantial Stokes shift (~150 nm) confirmed strong electron–phonon coupling, a hallmark of STE systems, while the maximum emission intensity was achieved under excitation at 450 nm, consistent with the material's absorption profile. Owing to these properties, the compound shows promise for applications in optical detectors, light-emitting diodes (LEDs), and solid-state luminescent devices.

Impedance spectroscopy conducted between 313 and 363 K revealed thermally activated conduction behavior with a negative temperature coefficient of resistance (NTCR). The AC conductivity followed Jonscher's universal power law, and analysis of the charge transport mechanism clearly demonstrated that conduction was dominated by the nonoverlapping small polaron tunneling (NSPT) mechanism. Analysis of the complex dielectric modulus revealed non-Debye relaxation behavior. The stretching parameter β increased with the temperature, indicating a gradual transition toward more ideal relaxation dynamics at elevated temperatures. The activation energies derived from AC conductivity (E_a = 0.47 eV) and relaxation frequency (E_a = 0.49 eV) were in close agreement, indicating that both ion transport and relaxation dynamics were governed by the same energy barrier, primarily associated with the thermally activated motion of $(CH_3NH_3)^+$ cations.

Collectively, these findings establish $(CH_3NH_3)_3(SbCl_5)\cdot Cl$ as a promising candidate for fundamental optoelectronic studies and underscore the critical role of the crystal structure, hydrogen-bonding interactions, and structural defects in governing the material's electrical and optical properties.

Conflicts of interest

There are no conflicts to declare.

Data availability

All data supporting the findings of this study are included within the manuscript.

Supplementary information (SI): Table S1: anisotropic displacement parameters ($Å^2 \times 10^3$) for $[(CH_6N)_3(SbCl_5)\cdot Cl]$; Table S2: fractional atomic coordinates ($\times 10^4$) and equivalent isotropic displacement parameters ($Å^2 \times 10^3$) for $[(CH_6N)_3(SbCl_5)\cdot Cl]$. U_{eq} is defined as 1/3 of the trace of the orthogonalised U_{ij} tensor and Table S3: bond length (Å) and angles (°) of compound$[(CH_6N)_3(SbCl_5)\cdot Cl]$. See DOI: https://doi.org/10.1039/d6ra00964f.

CCDC 2443838 contains the supplementary crystallographic data for this paper.[57]

Acknowledgements

The Gobierno del Principado de Asturias (IDE/2024/000742) and the University of Salamanca (K257-463AC01) are acknowledged. The authors extend their appreciation to the Scientific and Technical Services (STSs) staff at the University of Oviedo for their support in elaborating this work.

References

1 M. Khalid and T. K. Mallick, Stability and Performance Enhancement of Perovskite Solar Cells: A Review, *Energies*, 2023, **16**, 4031.
2 https://www.nrel.gov/ncpv/images/efficiency_chart.jpg, 2016.
3 C. Geffroy, E. Grana, T. Bessho, S. Almosni, Z. Tang, A. Sharma, T. Kinoshita, F. Awai, E. Cloutet, T. Toupance, H. Segawa and G. Hadziioannou, *ACS Appl. Energy Mater.*, 2020, **3**, 1393–1401.
4 J. Huang, Y. Yuan, Y. Shao and Y. Yan, *Nat. Rev. Mater.*, 2017, **2**, 17042.
5 S. Mahesh, J. M. Ball, R. D. J. Oliver, D. P. McMeekin, P. K. Nayak, M. B. Johnston and H. J. Snaith, *Energy Environ. Sci.*, 2020, **13**, 258–267.
6 T. Baikie, N. S. Barrow, Y. Fang, P. J. Keenan, P. R. Slater, R. O. Piltz, M. Gutmann, S. G. Mhaisalkar and T. J. White, *J. Mater. Chem.*, 2015, **3**, 9298–9307.
7 X. Ma, F. Zhang, Z. Chu, J. Hao, X. Chen, J. Quan, Z. Huang, X. Wang and X. Li, *Nat. Commun.*, 2021, **12**, 1234.
8 J. Avila, C. Momblona, P. P. Boix, M. Sessolo and H. J. Bolink, *Joule*, 2017, **1**, 431–442.
9 A. D. Nicholas, *J. Phys. Chem. C*, 2020, **124**, 24485–24494.
10 R. Jakubas, *et al.*, *RSC Adv.*, 2021, **11**, 1217–1225.
11 J. Zhang, Y. Yang, H. Deng, Z. Mao, H. Zhong, Z. Xu and X. Lin, *ACS Nano*, 2017, **11**, 9294–9302.
12 M. Bujak and J. Zaleski, *J. Mol. Struct.*, 2003, **647**, 121–128.
13 K. Kahouli, *et al.*, *Indian J. Phys.*, 2022, 2797–2805.
14 W. Boujelbene, *et al.*, *J. Mater. Sci.: Mater. Electron.*, 2025, **36**, 936.
15 K. Guithi, *et al.*, *J. Opt.*, 2023, **52**, 1494–1506.
16 H. Chen, *et al.*, *Appl. Phys. Lett.*, 2021, 119–052901.
17 Y. Gao, *et al.*, *ACS Appl. Mater. Interfaces*, 2022, **14**, 5678–5685.
18 G. M. Sheldrick, *SHELXL 2018*, University of Göttingen, 2018.
19 M. J. Wallis, H. M. Tairo, M. M. Bhadbhade, R. Tian, L. F. Lindoy and F. Li, *Cryst. Growth Des.*, 2023, **23**, 1404.
20 A. Kumar and R. K. Singh, Dielectric and AC conduction studies of lead-free halide perovskites, *J. Alloys Compd.*, 2020, **823**, 153735.
21 X.-Z. Li, *J. Appl. Crystallogr.*, 2026, **82**, 14–21.
22 M. Webster and S. Keats, *J. Chem. Soc. A*, 1971, 298–299.
23 T. Ben Rhaiem and H. Boughzala, *Acta Crystallogr., Sect. E:Crystallogr. Commun.*, 2015, **71**, 498–501.
24 M. Bujak and J. A. Ross, *J. Solid State Chem.*, 2005, **178**, 2237–2246.
25 S. V. Motloung, M. Tsega, F. B. Dejene, H. C. Swart, O. M. Ntwaeaborwa, L. F. Koao, T. E. Motaung and M. J. Hato, *J. Alloys Compd.*, 2016, **677**, 72–79.

26 J. Klein, L. Kampermann, B. Mockenhaupt, M. Behrens, J. Strunk and G. Bacher, *Adv. Funct. Mater.*, 2023, **33**, 2304523.
27 P. Kubelka and F. Munk, *Leaf Optical Properties*, 2019, pp. 455–461.
28 A. S. Hassanien, A. A. Akl and I. M. El Redaf, Optical characteristics of the novel nanosized thin $ZnGa_2S_4$ films sprayed at different deposition times: determination of optical band-gap energy using different methods, *Emergent Mater.*, 2023, **6**, 943–964, DOI: 10.1007/s42247-023-00493-0.
29 S. M. Rozati and S. A. M. Ziabar, A review of various single layer, bilayer, and multilayer transparent conducting oxide (TCO) materials and their applications, *Mater. Chem. Phys.*, 2022, **292**, 126789, DOI: 10.1016/j.matchemphys.2022.126789.
30 A. Amin, N. Elleuch, A. Oueslati, S. Shovac and M. Boujelbene, *RSC Adv.*, 2025, **15**, 45840.
31 M. Li, P. Huang and H. Zhong, *J. Phys. Chem. Lett.*, 2023, **14**, 1592–1603.
32 S. K. Nahar and P. Kumar, *J. Mater. Sci.: Mater. Electron.*, 2020, **31**, 15722–15732.
33 N. Chakchouk, D. R. Almalawi, I. H. Smaili, F. Aljuaid and A. Ben Rhaiem, Title of the Article, *Appl. Organomet. Chem.*, 2024, **38**, 15.
34 A. C. Dhieb, A. Valkonen, M. Rzaigui and W. Smirani, *J. Mol. Struct.*, 2015, **1102**, 50–56.
35 H. Lin, Q. Wei, B. Ke, W. Lin, H. Zhao and B. Zou, *J. Phys. Chem. Lett.*, 2023, **14**, 1460–1469.
36 G. Chen, X. Guo, H. Lin, Z. Zhang, A. Ablez, Y. Ren, K. Du and X. Huang, *Molecules*, 2025, **20**, 3016–3431.
37 G. Krishnamurthy Grandhi, R. Dhama, N. Srinivasa Manikanta Viswanath, E. S. Lisitsyna, B. Al-Anesi, J. Dana, H. C. VipinrajSugathan and P. Vivo, *J. Phys. Chem. Lett.*, 2023, **14**, 4192–4199.
38 R. Zhang, H. Xie, Q. Zhao, Z. Tang, C. Yang and B. Su, *Inorg. Chem.*, 2023, **62**(48), 19771–19779.
39 Z. Li, Y. Li, P. Liang, T. Zhou, L. Wang and R.-J. Xie, *Chem. Mater.*, 2019, **31**(22), 9363–9371.
40 H. Lin, Q. Wei, B. Ke, W. Lin, H. Zhao and B. Zou, *Adv. Opt. Mater.*, 2021, **9**(8), 2002213.
41 M. B. Bechir and F. Alresheedi, *RSC Adv.*, 2023, **13**, 34703–34714.
42 M. B. Bechir and M. H. Dhaou, *Mater. Res. Bull.*, 2021, **144**, 111473.
43 A. K. Panda, L. Sahoo, N. C. Nayak, B. N. Parida and R. K. Parida, *J. Mater. Sci.: Mater. Electron.*, 2023, **34**, 1640, DOI: 10.1007/s10854-023-11045-x.
44 M. Beltaif, M. Krichen, M. Megdiche and M. Dammak, *Ionics*, 2019, **25**, 3247–3258.
45 R. N. Bhowmik and A. G. Lone, *J. Alloys Compd.*, 2016, **680**, 31–42.
46 S. Pandey, D. Kumar, O. Parkash and L. Pandey, *Integr. Ferroelectr.*, 2017, **183**, 141–162.
47 S. Fujii, T. Yokoi, C. A. Fisher, H. Moriwake and M. Yoshiya, *Nat. Commun.*, 2020, **11**, 1854.
48 Y. Yin, W. Tian, J. Leng, J. Bian and S. Jin, *J. Phys. Chem. Lett.*, 2020, **11**, 6956–6963.
49 N. Chakchouk, K. Karoui, N. Drissi, F. Jomni and A. Ben Rhaiem, *RSC Adv.*, 2024, **14**, 46–58, DOI: 10.1039/D3RA07453F.
50 A. Ghosh, *J. Appl. Phys.*, 2017, **122**, 215102.
51 Y. Yong, *Solid State Ionics Reviews*, 2025.
52 S. R. Elliott, Physics of amorphous materials, *J. Phys.: Condens. Matter*, 2018, **30**, 343001.
53 M. Ben Bechir and M. HoucineDhaou, *Mater. Res. Bull.*, 2021, 144–111473, DOI: 10.1016/j.materresbull.2021.111473.
54 A. Kumar and R. K. Singh, Dielectric and AC conduction studies of lead-free halide perovskites, *J. Alloys Compd.*, 2020, **823**, 153735.
55 K. Holderna-Natkaniec, M. O. M. Sghaier, P. Ławniczak, M. Zdanowska-Fraczek, A. Wozniak-Braszak and S. Chaabouni, *Polyhedron*, 2015, **85**, 131–136.
56 A. A. Alnafea, N. Chakchouk, H. A. Siddiq, S. M. Altarifi, M. H. Dhaou and A. B. Rhaiem, *Appl. Organomet. Chem.*, 2025, **39**, e70088, DOI: 10.1002/aoc.70088.
57 CCDC 2443838: Experimental Crystal Structure Determination, 2026, DOI: 10.5517/ccdc.csd.cc2n10h7.